PIBB 生物化学与生物物理进展
Progress in Biochemistry and Biophysics
2025, 52(8): 2163~2172
www.pibb.ac.cn

Predicting Hepatocellular Carcinoma Using Brightness Change Curves Derived From Contrast-enhanced Ultrasound Images*

CHEN Ying-Ying[1)], JIANG Shang-Lin[1)], HUANG Liang-Hui[1)], ZENG Ya-Guang[1)], WANG Xue-Hua[1)**], ZHENG Wei[2)**]

([1)]*School of Physics and Optoelectronic Engineering, Foshan University, Foshan* 528225, China;
[2)]*State Key Laboratory of Oncology in South China, Collaborative Innovation Center of Cancer Medicine, Department of Ultrasound, Sun Yat-sen University Cancer Center, Guangzhou* 510060, China)

Abstract **Objective** Primary liver cancer, predominantly hepatocellular carcinoma (HCC), is a significant global health issue, ranking as the sixth most diagnosed cancer and the third leading cause of cancer-related mortality. Accurate and early diagnosis of HCC is crucial for effective treatment, as HCC and non-HCC malignancies like intrahepatic cholangiocarcinoma (ICC) exhibit different prognoses and treatment responses. Traditional diagnostic methods, including liver biopsy and contrast-enhanced ultrasound (CEUS), face limitations in applicability and objectivity. The primary objective of this study was to develop an advanced, light-weighted classification network capable of distinguishing HCC from other non-HCC malignancies by leveraging the automatic analysis of brightness changes in CEUS images. The ultimate goal was to create a user-friendly and cost-efficient computer-aided diagnostic tool that could assist radiologists in making more accurate and efficient clinical decisions. **Methods** This retrospective study encompassed a total of 161 patients, comprising 131 diagnosed with HCC and 30 with non-HCC malignancies. To achieve accurate tumor detection, the YOLOX network was employed to identify the region of interest (ROI) on both B-mode ultrasound and CEUS images. A custom-developed algorithm was then utilized to extract brightness change curves from the tumor and adjacent liver parenchyma regions within the CEUS images. These curves provided critical data for the subsequent analysis and classification process. To analyze the extracted brightness change curves and classify the malignancies, we developed and compared several models. These included one-dimensional convolutional neural networks (1D-ResNet, 1D-ConvNeXt, and 1D-CNN), as well as traditional machine-learning methods such as support vector machine (SVM), ensemble learning (EL), k-nearest neighbor (KNN), and decision tree (DT). The diagnostic performance of each method in distinguishing HCC from non-HCC malignancies was rigorously evaluated using four key metrics: area under the receiver operating characteristic (AUC), accuracy (ACC), sensitivity (SE), and specificity (SP). **Results** The evaluation of the machine-learning methods revealed *AUC* values of 0.70 for SVM, 0.56 for ensemble learning, 0.63 for KNN, and 0.72 for the decision tree. These results indicated moderate to fair performance in classifying the malignancies based on the brightness change curves. In contrast, the deep learning models demonstrated significantly higher *AUC*s, with 1D-ResNet achieving an *AUC* of 0.72, 1D-ConvNeXt reaching 0.82, and 1D-CNN obtaining the highest *AUC* of 0.84. Moreover, under the five-fold cross-validation scheme, the 1D-CNN model outperformed other models in both accuracy and specificity. Specifically, it achieved accuracy improvements of 3.8% to 10.0% and specificity enhancements of 6.6% to 43.3% over competing approaches. The superior performance of the 1D-CNN model highlighted its potential as a powerful tool for accurate

* This work was supported by grants from The National Natural Science Foundation of China (62075042, 62205060, 82202179), Medical Scientific Research Fundation of Guangdong Province (A2020306), and Special Fund for Science and Technology Innovation Cultivation of Guangdong University Students (pdjh2024a387).
** Corresponding author.
WANG Xue-Hua. Tel: 86-757-82716895, E-mail: xhwang10000@163.com
ZHANG Wei. Tel: 86-20-87343212, E-mail: zhengwei@sysucc.org.cn
Received: December 11, 2024 Accepted: April 27, 2025

classification. **Conclusion** The 1D-CNN model proved to be the most effective in differentiating HCC from non-HCC malignancies, surpassing both traditional machine-learning methods and other deep learning models. This study successfully developed a user-friendly and cost-efficient computer-aided diagnostic solution that would significantly enhances radiologists' diagnostic capabilities. By improving the accuracy and efficiency of clinical decision-making, this tool has the potential to positively impact patient care and outcomes. Future work may focus on further refining the model and exploring its integration with multimodal ultrasound data to maximize its accuracy and applicability.

Key words computer-aided diagnostic, deep learning, hepatocellular carcinoma, contrast-enhanced ultrasound, brightness change curve

DOI：10.16476/j.pibb.2024.0517 **CSTR**：32369.14.pibb.20240517

Primary liver cancer ranks as the sixth most commonly diagnosed cancer globally and is the third leading cause of cancer-related mortality. This category consists predominantly of hepatocellular carcinoma (HCC), accounting for 75%−85% of cases; intrahepatic cholangiocarcinoma (ICC), comprising 10%−15% of cases; and other rare types[1]. HCC has a more favorable prognosis and is usually treated with local ablation techniques, such as radiofrequency and transarterial chemoembolization[2-3]. ICC, a major non-HCC liver malignancy, is characterized by aggressive behavior, treatment challenges, and poor prognosis. The primary curative treatment for ICC involves surgical methods, such as liver resection. In the clinical setting, ICC is easily misidentified as HCC or cancer of unknown primary origin[4-7]. Therefore, precise and early diagnosis of HCC is crucial for promptly initiating the correct treatment[2-3, 8].

Although a liver biopsy remains the standard method for HCC diagnosis, it is often unnecessary in patients with typical imaging characteristics of focal lesions[2-3, 9]. Contrast-enhanced ultrasound (CEUS) is a commonly employed imaging modality for detecting and assessing tumor blood flow perfusion in HCC because of its operational simplicity, immediate results, non-invasiveness, absence of radiation exposure, and portability[9-11]. It effectively visualizes the blood supply to the tumor and its adjacent liver tissue, offering insightful hemodynamic information for differential liver cancer diagnosis[2-3]. HCC is generally diagnosed using CEUS features following standard guidelines, including typical arterial phase hyperenhancement and late washout onset (greater than or equal to 60 s) with mild washout intensity[8, 10]. Washout onset typically occurs within 1 min, sooner in ICC than that in HCC. In addition, the washout degree is more pronounced in ICC than in HCC[10-13]. Radiologists' interpretation of features, such as enhancement and washout intensity, is highly subjective and requires extensive training. Diagnostic accuracy is significantly influenced by the radiologist's experience and expertise[14-16].

Using time-intensity curve (TIC) analysis to interpret CEUS videos effectively solves diagnostic challenges[17]. This method involves manually plotting and comparing the average intensity levels on a timescale for the following two specific areas identified by radiologists: within the suspected tumor and in a parenchymal region devoid of significant vessels. This process generates two curves depicting the contrast uptake during CEUS[18]. This method provides accurate brightness quantification on CEUS, thereby assisting in a more precise diagnosis[15]. Pei *et al*.[19] used software to generate TICs and extracted 4 quantitative parameters (time-to-peak, rising slope, maximum intensity, and rising time) to differentiate between focal nodular hyperplasia and HCC. The results indicate that this method can enhance diagnostic accuracy beyond the capabilities of standard CEUS examinations. Moreover, it is more advantageous for differential diagnosis than analyzing hemodynamics alone[19].

Numerous computer-aided diagnostic systems using TIC analysis have emerged recently to support clinicians[20-21]. For example, Liu *et al*.[22] extracted 18 quantitative parameters related to time, intensity, and velocity from TICs and used a support vector machine (SVM) to predict the response of forecasts with HCC to hepatic artery chemoembolization with 81.0% accuracy. Similarly, Kondo *et al*.[16] trained an SVM classifier using 28 manually selected features, including TIC and enhancement morphology parameters, achieving an accuracy of 87.7% for HCC across three classifications. Streba *et al*.[18] analyzed TICs to categorize HCC and 4 additional liver diseases. These methods typically rely on the

empirical determination of features and experimentally established parameters. Unlike methods relying on manually defining features, deep-learning methods use unsupervised feature learning. For example, Wu *et al*.[23] implemented deep belief networks to differentiate between benign and malignant focal liver lesions using TIC analysis. Their results indicated that the performance of the deep learning approach surpasses that of conventional machine learning methods.

These studies demonstrate the effectiveness of the automated TIC analysis as a valuable technique, offering clinicians rapid and dependable diagnostic support[18]. However, existing methods for HCC classification have several limitations. Labeling tumor regions manually on B-mode ultrasound (BUS) and CEUS images requires extensive clinical expertise and significant time investment by radiologists[24], and outcomes are influenced by an individual radiologist's subjective experience[16]. Machine-learning classification methods often depend on handcrafted features that limit the extraction of a wide range of features and end-to-end learning[24]. No deep learning models have been designed specifically to analyze the brightness change curves to differentiate HCC from non-HCC malignancies.

To overcome these limitations, we used a YOLOX network[25] to identify the region of interest (ROI), including the tumor and adjacent normal liver tissues, on the BUS images. We then extracted brightness change curves from CEUS images using a custom-developed algorithm, which depicts immediate temporal brightness variations in the tumor and liver parenchyma. We also developed one-dimensional convolutional neural network (1D-CNN) models and used several traditional machine-learning methods to explore their capability to differentiate HCC from non-HCC malignancies by analyzing brightness change curves.

1 Materials and methods

1.1 Patients

The retrospective study protocol was approved by the Human Research Ethics Committee of Sun Yat-sen University Cancer Center (approval number: GYX2020-017) and adhered to the tenets of the Declaration of Helsinki. Only anonymized retrospective data were used for research. We gathered data from patients diagnosed with liver cancer who underwent CEUS at the Sun Yat-sen University Cancer Center. The inclusion criteria for this study were: (1) patients presenting with hypervascular liver nodules as verified through CEUS; (2) available BUS and CEUS data; (3) lesions confirmed to be HCC *via* histological analysis or identified as non-HCC based on histological or clinical evidence. The exclusion criteria were: (1) patients who had received chemotherapy, interventional treatment, or local treatment; (2) patients whose CEUS videos shook excessively; (3) difficult tumor location; (4) tumors obscured by shadows; (5) tumors extended beyond the view boundary. Based on these criteria, 161 patients were included in this study. The cohort included 131 HCC cases (121 males and 10 females, aged (52±12.38) years) and 30 non-HCC malignancies (15 males and 15 females, aged (51.23±10.43) years). In the HCC group, 5.34% (7 patients) had multiple tumors, and 99.2% were >10 mm in diameter. Similarly, 26.7% (8 patients) in the non-HCC group had multiple tumors, with 91.7% exceeding 10 mm.

1.2 Ultrasound data collection

BUS examinations were performed by expert radiologists specializing in abdominal imaging using the Acuson Sequoia 512 system (Siemens; Mountain View, CA, USA). The quantification of the lesions, including their count, dimensions, spatial distribution, and sonographic appearance, as well as the characteristics of the hepatic backdrop, was meticulously recorded. CEUS was performed by using a 4C1 convex array probe (Siemens). Low-mechanical index CEUS, with a dynamic range set to 80 dB, was conducted subsequent to the intravenous administration of 2.0 ml of SonoVue contrast agent (Bracco Imaging; Milan, Italy), followed by a saline solution flush of 5 ml. A timer was started when the contrast agent was injected. Imaging was recorded at 8 frames/s on cine clips for 80 s. After an 80-second interval, the lesion underwent periodic scanning over a 5-min duration to delineate washout characteristics.

1.3 ROI extraction

This study employs YOLOX network[26] to automatically label tumor ROI. This model consists of 5 fundamental components: the input, feature extraction, convolution block attention module, feature fusion, and prediction. It outputs the tumor's central coordinates (x, y) and delineates its dimensions

using a bounding box, which was used to obtain the ROI on the BUS images (Figure 1a). These coordinates were mapped directly on CEUS, and superfluous borders were removed systematically. The identified ROI encompassed the tumor and a portion of the surrounding liver parenchyma. We defined the 8 corners as the liver parenchyma region, constituting 1% of the ROI, and the remainder as the tumor (Figure 1b). The dataset contains a total of 4 830 BUS images, which are divided into training, verification and prediction sets in the ratio of 6∶2∶2. The YOLOX annotation results were manually verified by experienced radiologists. The YOLOX demonstrated an accuracy of 95.13% in test set, confirming its superior capability in identifying liver tumors and their surrounding tissues.

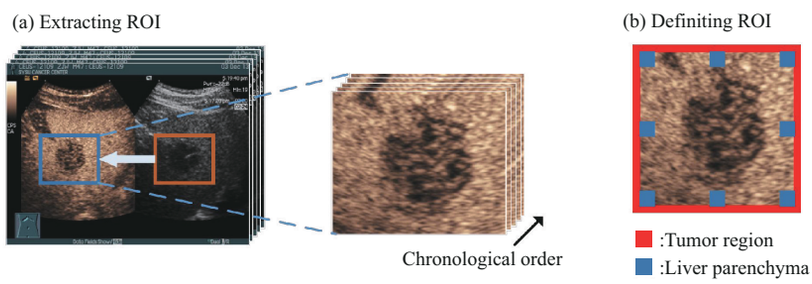

Fig. 1 Region of interest (ROI) extraction

(a) Extracting ROI on BUS and CEUS. (b) The blue area is defined as the liver parenchyma; the remaining area is defined as the tumor. ROI: region of interest.

1.4 Generating the brightness change curves dataset

The production process comprised the following steps.

(1) CEUS ROIs were converted to grayscale and organized chronologically. The pixel values were averaged over the tumor and liver parenchyma regions, generating two curves representing the brightness change over time.

(2) Gaussian filtering and cubic spline interpolation were used to refine the curves. Besides, refer to the radiologists' diagnostic protocols[2, 9-10], the first 180-second brightness change curve (Figure 2) were intercepted, for this time window can effectively capture the brightness variation of tumor, while minimize the redundant information.

(3) The quantitative parameters for the machine-learning methods were derived from the brightness change curves. For example, the CEUS4 dataset[19] was formed by extracting the following four features: time to peak, rising slope, maximum intensity, and rising time. The TJ18 dataset[22] was constructed by extracting 18 important features, including 5 time-related features, 6 intensity-related features, and 7 speed-related features.

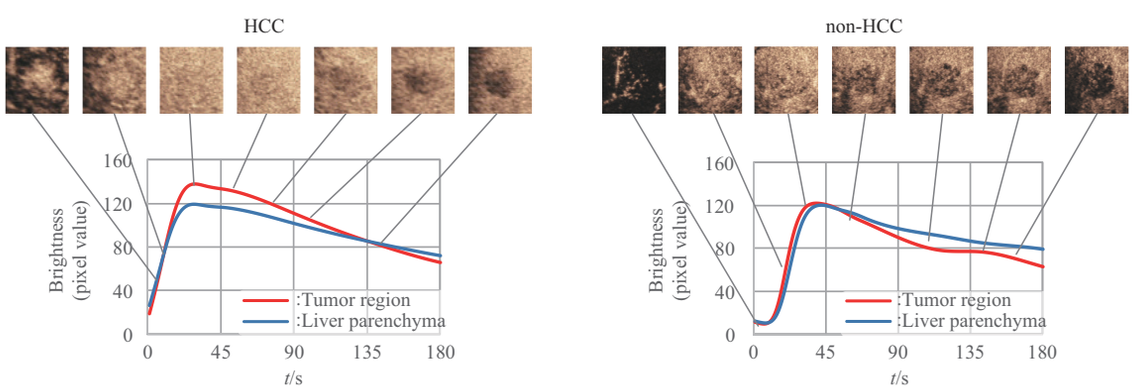

Fig. 2 Examples of brightness change curves for HCC and non−HCC cases

The red curves indicate the brightness change in the tumor region over time. The blue curves indicate the brightness change in the liver parenchyma region over time.

(4) To emulate the radiologist's diagnostic pattern of comparing the brightness changes in the tumor and liver parenchyma[19, 23], the two brightness change curves were divided point-by-point to generate a third composite curve. These curves were inputted into a 1D-CNN model for training and verification.

1.5 Building the classification models

This study developed 3 deep learning models and four machine-learning methods to differentiate HCC from non-HCC malignancies by analyzing the brightness change curves (Figure 3).

The architecture of 1D-CNN is depicted in Figure 4. It encompasses four 1D convolutional layers and a 1D pooling layer. Convolutional layers were employed to extract features from the input curves. The pooling layer reduces the computational demands and minimizes the influence of nonessential information[27]. Batch normalization was implemented following each convolutional layer, which can significantly accelerate training and improve the learning rate[28]. The softmax and LeakyReLU activation functions were applied after batch normalization. Global average pooling condenses multichannel features into a 1D vector[27, 29]. A dropout layer was implemented with a dropout rate set at 0.2 to mitigate the risk of overfitting. The final layer was equipped with a sigmoid activation layer to generate scores to distinguish between HCC and non-HCC cases.

Besides, two mainstream deep learning models, Residual Network (ResNet) [30] and ConvNeXt[31], were converted into one-dimensional classification networks, designated as 1D-ResNet and 1D-ConvNeXt, respectively, and 4 machine learning methods: SVM[32], ensemble learning (EL) [33], K-nearest neighbor (KNN) [34], decision tree (DT) [35], have been developed to classify HCC and non-HCC under the same datasets.

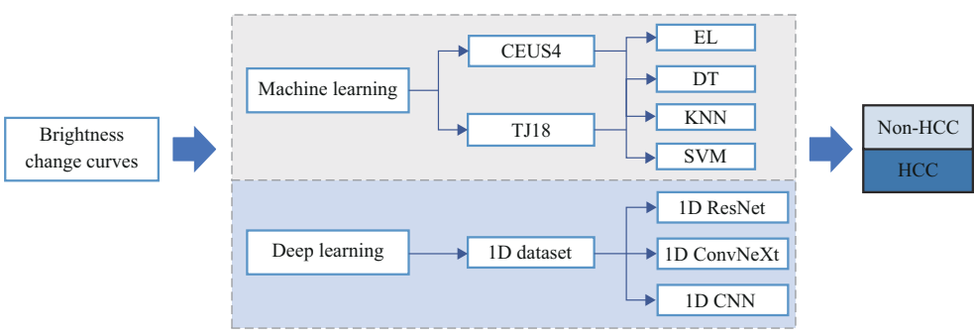

Fig. 3 Schematic diagram of the analysis of the brightness change curves

CEUS4: a machine learning dataset called CEUS4; TJ18: a machine learning dataset called TJ18; EL: ensemble learning; DT: decision tree; KNN: K-nearest neighbor; SVM: support vector machine; CNN: convolutional neural network.

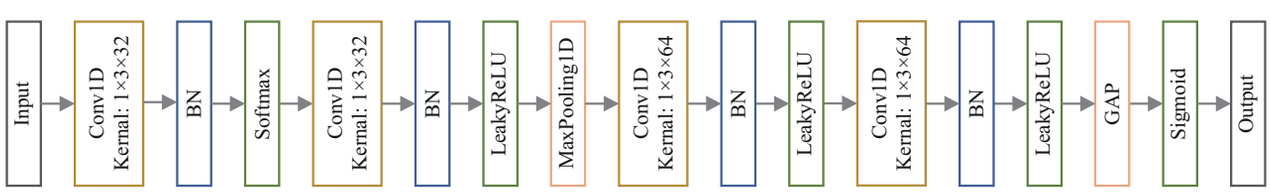

Fig. 4 Architecture diagram of a 1D−CNN model

Conv 1D: one-dimensional convolutional layer, BN: batch normalization, GAP: global average pooling.

1.6 Experimental design and analysis scheme

The computational experiments were conducted on a laptop equipped with a 64-bit Windows 10 operating system, 16 GB of RAM, and an AMD Ryzen 5 5500U processor with integrated Radeon Graphics, operating at a base frequency of 2.10 GHz. The machine learning classification models were developed using MATLAB's Classification Learner

application (R2022a), while the deep learning models were designed using the Keras framework in the Python 3.6 environment.

The 1D-CNN model contains 22 882 parameters, representing a 91.45% reduction compared to the benchmark 1D-ResNet model, which has 267 618 parameters. In terms of computational speed, our method processed 32 cases in just 0.265 s. The model's weight storage space is only 338 KB.

Metrics of area under the receiver operating characteristic curves (AUC), accuracy, sensitivity, and specificity, were used to assess the effectiveness of the classification models. The closer the *AUC* is to 1.0, the better the model performs. Accuracy quantifies the ratio of correctly classified samples to the total sample count, corresponding to the model's overall classification power. Sensitivity and specificity measure the model's accuracy in correctly identifying HCC and non-HCC cases. These indicators are calculated by the following formulas:

$$Accuracy = \frac{TP + TN}{TP + FP + TN + FN} \quad (1)$$

$$Sensitivity = \frac{TP}{TP + FN} \quad (2)$$

$$Specificity = \frac{TN}{TN + FP} \quad (3)$$

$$AUC = \int_0^1 t_{pr}(f_{pr})\mathrm{d}f_{pr} = P \quad (4)$$

Among them, TP, TN, FP, and FN represent the quantities of true positives, true negatives, false positives, and false negatives, respectively. t_{pr}denotes the true positive rate, f_{pr} denotes the false positive rate, and t_{pr} is a function of f_{pr}. All models underwent fivefold cross-validation to ensure the stability of the classification results. The datasets were divided into training and testing sets with an 8∶2 ratio. In each trial, 129 of the 161 participants were allocated to the training set, and 32 were designated for testing.

2 Results

The performance metrics of the 1D-CNN models and machine learning methods, including accuracy, sensitivity, and specificity, are summarized in Table 1. The results are presented as average values with corresponding ranges and 95% confidence intervals. In the testing cohort, the 1D-CNN model achieved an accuracy of 83.9%, sensitivity of 89.3%, and specificity of 60.0% in distinguishing HCC from non-HCC malignancies.

Compared to traditional machine learning methods, the 1D-CNN model demonstrated significant improvements in accuracy (increased by 5.6%−10.0%) and specificity (increased by 23.3%−43.3%), although its sensitivity was 1.5% lower than that of the DT method. Moreover, the 1D-CNN outperformed the 1D-ResNet and 1D-ConvNeXt models in terms of accuracy (enhanced by 3.8%−5.6%), sensitivity (enhanced by 2.3%−5.3%), and specificity (enhanced by 6.6%−10.0%).

As illustrated in Figure 5, the *AUC* values for EL, DT, KNN, SVM, 1D-ResNet, 1D-ConvNeXt, and 1D-CNN were 0.70, 0.56, 0.63, 0.72, 0.72, 0.82, and 0.84, respectively. These results indicate that the 1D-CNN model exhibits best overall performance among the evaluated methods. Notably, the substantial increase in specificity achieved by the 1D-CNN can significantly reduce the rate of misdiagnosis of HCC, thereby enhancing diagnostic reliability.

Table 1 Comparison of performance metrics between the EL, DT, KNN, SVM, and 1D−CNN, 1D−ResNet, 1D−ConvNeXt models in testing cohorts

Model	Accuracy/%	Sensitivity/%	Specificity/%
EL	77.0 (71.7−82.4)	87.0 (73.8−100)	33.4 (1.9−64.8)
DT	77.0 (75.3−78.7)	**90.8 (87.4−94.1)**	16.7 (0.65−32.7)
KNN	73.9 (72.4−75.5)	84.7 (81.6−87.9)	26.7 (10.8−42.6)
SVM	78.3 (70.1−86.5)	87.8 (81.2−94.4)	36.7 (19.8−53.5)
1D-ResNet	80.1 (70.3−89.9)	87.0 (75.4−98.6)	50.0 (35.4−64.6)
1D-ConvNeXt	78.3 (68.2−88.2)	84.0 (71.6−96.3)	53.3 (30.6−76.0)
1D-CNN **(in this study)**	**83.9 (78.0−89.6)**	89.3 (82.5−96.0)	**60.0 (50.4−69.6)**

The 95% confidence intervals for quantitative data are indicated in brackets when applicable. EL: ensemble learning; DT: decision tree; KNN: K-nearest neighbor; SVM: support vector machine; 1D-ResNet: one-dimensional residual network; 1D-ConvNeXt: one-dimensional ConvNeXt; 1D-CNN: one-dimensional convolutional neural network.

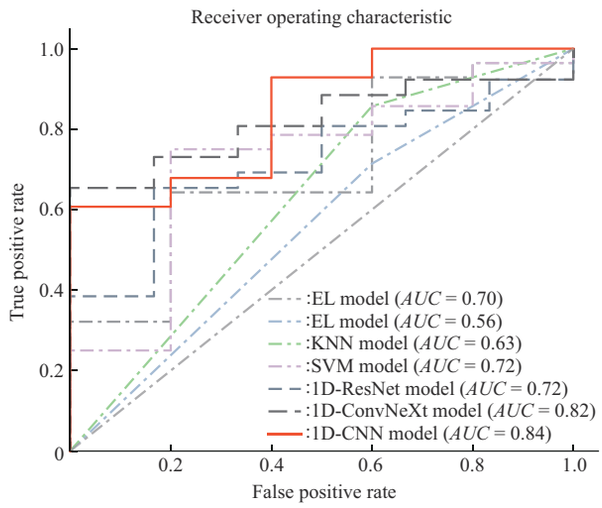

Fig. 5 The receiver operating characteristic curves of EL, DT, KNN, SVM, 1D−CNN, 1D−ResNet and 1D−ConvNeXt models in the testing cohort

3 Discussion

In this section, we will explore 4 key topics: the differences between brightness change curves and TIC curves, the advantages of our approach compared to 2D and 3D liver cancer classification models, the reasons for the lower specificity in HCC and non-HCC classification, and the limitations of this study.

TIC and brightness change curves are two methods for analyzing CEUS. TIC relies on manual ROI delineation by radiologists, which is subjective and time-consuming, focusing on early-phase perfusion within the first 60 s. In contrast, brightness change curves use YOLOX for automatic annotation, enabling real-time analysis with an extended 180-second acquisition window. This captures comprehensive tumor perfusion dynamics, including late-phase washout. The automated approach enhances consistency and diagnostic accuracy, especially in distinguishing HCC from non-HCC malignancies.

A lot of 2D and 3D-CNN models have been recently applied to liver cancer classification[36-37]. However, these experiments have limitations. For example, they require manual ROI labeling by radiologists and substantial data storage, computational volume, and computational complexity[38]. The present study used YOLOX to automate the annotation of ROIs and one-dimensional brightness change curves for HCC and non-HCC classification, requiring less memory and computational resources. Our method reduces the equipment requirements for model training and enhances the model's suitability for implementation in medical devices.

Besides, our 1D-CNN model proposed in this study exhibited 60.0% specificity for classifying HCC from non-HCC, which is slightly lower than that reported in comparable liver cancer studies[16, 18-19, 22-23]. We attributed these differences to the following two factors: (1) differentiating HCC from non-HCC based solely on imaging data is clinically challenging for radiologists[4-7], and (2) non-HCC belongs to a rare cancer category[4-6], and experiments face challenges due to insufficient non-HCC data. Nevertheless, our 1D-CNN model outperformed the machine learning models. This superior performance can be attributed to the 1D-CNN model's capability to automatically learn discriminative features from the brightness change curves[23-24].

This study had a few limitations. The sample size was small, and patients evaluated at multiple centers with different instruments were not included. This could potentially lead to the model's diminished ability to generalize, an over-reliance on the sampling instrument, and a lack of model specificity. Moving forward, we aim to gather more robust and extensive case data to enhance the model's training, thereby addressing the issue at hand. Our findings are preliminary. However, our model can be integrated with the BUS and CEUS models to establish a multimodal ultrasound network for improved HCC detection.

4 Conclusion

This study presents an innovative automated diagnostic method for differentiating HCC from non-HCC cases. The system integrates advanced technologies to address key challenges: it uses the YOLOX network for automatic ROI labeling, generates brightness change curves without manual parameter extraction, and employs a lightweight 1D-CNN to reduce computational costs. The 1D-CNN outperforms traditional machine learning methods, with improvements of 5.6%−10.0% in accuracy, 23.3%−43.3% in specificity, and 0.12−0.28 in AUC. It also surpasses previous 1D-ResNet and 1D-

ConvNeXt models by 3.8%−5.6% in accuracy, 2.3%−5.3% in sensitivity, and 6.6%−10.0% in specificity. This practical system could be integrated into medical devices to aid clinical radiologists in accurately distinguishing HCC from non-HCC patients.

References

[1] Bray F, Laversanne M, Sung H, *et al*. Global cancer statistics 2022: GLOBOCAN estimates of incidence and mortality worldwide for 36 cancers in 185 countries. CA Cancer J Clin, 2024, **74**(3): 229-263

[2] National Health Commission of the People's Republic of China. Standard for diagnosis and treatment of primary liver cancer (2024 edition). J Clin Hepatol, 2024, **40**(5): 893-918

[3] Zhou J, Sun H, Wang Z, *et al*. Guidelines for the diagnosis and treatment of hepatocellular carcinoma (2019 edition). Liver Cancer, 2020, **9**(6): 682-720

[4] Brindley P J, Bachini M, Ilyas S I, *et al*. Cholangiocarcinoma. Nat Rev Dis Primers, 2021, **7**: 65

[5] Khan S A, Tavolari S, Brandi G. Cholangiocarcinoma: epidemiology and risk factors. Liver Int, 2019, **39**(Suppl 1): 19-31

[6] Bridgewater J, Galle P R, Khan S A, *et al*. Guidelines for the diagnosis and management of intrahepatic cholangiocarcinoma. J Hepatol, 2014, **60**(6): 1268-1289

[7] Ilyas S I, Khan S A, Hallemeier C L, *et al*. Cholangiocarcinoma - evolving concepts and therapeutic strategies. Nat Rev Clin Oncol, 2018, **15**(2): 95-111

[8] Dietrich C F, Nolsøe C P, Barr R G, *et al*. Guidelines and good clinical practice recommendations for contrast enhanced ultrasound (CEUS) in the liver-update 2020-WFUMB in cooperation with EFSUMB, AFSUMB, AIUM, and FLAUS. Ultraschall Med, 2020, **41**(5): 562-585

[9] Caraiani C, Boca B, Bura V, *et al*. Ct/MRI LI-RADS v2018 *vs*. CEUS LI-RADS v2017-can things be put together. Biology (Basel), 2021, **10**(5): 412

[10] Wilson S R, Lyshchik A, Piscaglia F, *et al*. CEUS LI-RADS: algorithm, implementation, and key differences from CT/MRI. Abdom Radiol (NY), 2018, **43**(1): 127-142

[11] de Sio I, Iadevaia M D, Vitale L M, *et al*. Optimized contrast-enhanced ultrasonography for characterization of focal liver lesions in cirrhosis: a single-center retrospective study. United European Gastroenterol J, 2014, **2**(4): 279-287

[12] Wildner D, Bernatik T, Greis C, *et al*. CEUS in hepatocellular carcinoma and intrahepatic cholangiocellular carcinoma in 320 patients-early or late washout matters: a subanalysis of the DEGUM multicenter trial. Ultraschall Med, 2015, **36**(2): 132-139

[13] Zheng W, Li Q, Zou X B, *et al*. Evaluation of contrast-enhanced US LI-RADS version 2017: application on 2020 liver nodules in patients with hepatitis B infection. Radiology, 2020, **294**(2): 299-307

[14] Dong Y, Wang W P, Mao F, *et al*. Application of imaging fusion combining contrast-enhanced ultrasound and magnetic resonance imaging in detection of hepatic cellular carcinomas undetectable by conventional ultrasound. J Gastroenterol Hepatol, 2016, **31**(4): 822-828

[15] Huang Q, Pan F, Li W, *et al*. Differential diagnosis of atypical hepatocellular carcinoma in contrast-enhanced ultrasound using spatio-temporal diagnostic semantics. IEEE J Biomed Health Inform, 2020, **24**(10): 2860-2869

[16] Kondo S, Takagi K, Nishida M, *et al*. Computer-aided diagnosis of focal liver lesions using contrast-enhanced ultrasonography with perflubutane microbubbles. IEEE Trans Med Imag, 2017, **36**(7): 1427-1437

[17] Goertz R S, Bernatik T, Strobel D, *et al*. Software-based quantification of contrast-enhanced ultrasound in focal liver lesions—a feasibility study. Eur J Radiol, 2010, **75**(2): e22-6

[18] Streba C T, Ionescu M, Gheonea D I, *et al*. Contrast-enhanced ultrasonography parameters in neural network diagnosis of liver tumors. World J Gastroenterol, 2012, **18**(32): 4427-4434

[19] Pei X Q, Liu L Z, Xiong Y H, *et al*. Quantitative analysis of contrast-enhanced ultrasonography: differentiating focal nodular hyperplasia from hepatocellular carcinoma. Br J Radiol, 2013, **86**(1023): 20120536

[20] Goceri E. Fully automated and adaptive intensity normalization using statistical features for brain MR images. Celal Bayar Üniversitesi Fen Bilimleri Dergisi, 2018, **14**(1): 125-134

[21] Huang Q, Zhang F, Li X. A new breast tumor ultrasonography CAD system based on decision tree and BI-RADS features. World Wide Web, 2018, **21**(6): 1491-1504

[22] Liu D, Liu F, Xie X, *et al*. Accurate prediction of responses to transarterial chemoembolization for patients with hepatocellular carcinoma by using artificial intelligence in contrast-enhanced ultrasound. Eur Radiol, 2020, **30**(4): 2365-2376

[23] Wu K, Chen X, Ding M. Deep learning based classification of focal liver lesions with contrast-enhanced ultrasound. Optik, 2014, **125**(15): 4057-4063

[24] Pan F, Huang Q, Li X. Classification of liver tumors with CEUS based on 3D-CNN//Ren H, Dobashi H, Wang Z, *et al*. 2019 IEEE 4th International Conference on Advanced Robotics and Mechatronics (ICARM). Toyonaka, Japan: IEEE, 2019: 845-849

[25] Ge Z, Liu S, Wang F, *et al*. YOLOX: exceeding YOLO series in 2021. arXiv, **2021**: 2107.08430. https://arxiv. org/abs/2107.08430v2

[26] Woo S, Park J, Lee J Y, *et al*. CBAM: convolutional block attention module//Ferrari V, Hebert M, Sminchisescu C, *et al*. Proceedings of The European Conference on Computer Vision (ECCV). Cham: Springer, 2018: 3-19

[27] Gu J, Wang Z, Kuen J, *et al*. Recent advances in convolutional neural networks. Pattern Recognit, 2018, **77**: 354-377

[28] Ioffe S, Szegedy C. Batch normalization: accelerating deep network training by reducing internal covariate shift. Proc Int Conf Mach Learn, 2015, **37**(2): 448-456

[29] Kumar R L, Kakarla J, Isunuri B V, *et al*. Multi-class brain tumor

classification using residual network and global average pooling. Multimed Tools Appl, 2021, **80**(9): 13429-13438

[30] He K, Zhang X, Ren S, *et al*. Deep residual learning for image recognition//Mortensen E, Saenko K. 2016 IEEE Conference on Computer Vision and Pattern Recognition (CVPR). Las Vegas, NV, USA: IEEE, 2016: 770-778

[31] Liu Z, Mao H, Wu C Y, *et al*. A ConvNet for the 2020s//Mortensen E. 2022 IEEE/CVF Conference on Computer Vision and Pattern Recognition (CVPR). New Orleans, LA, USA: IEEE, 2022: 11966-11976

[32] Hearst M A, Dumais S T, Osuna E, *et al*. Support vector machines. IEEE Intell Syst Appl, 1998, **13**(4): 18-28

[33] Sagi O, Rokach L. Ensemble learning: a survey. Wires Data Min Knowl Discov, 2018, **8**(4): e1249

[34] Erdogan S Z, Bilgin T T. A data mining approach for fall detection by using *k*-nearest neighbour algorithm on wireless sensor network data. IET Commun, 2012, **6**(18): 3281-3287

[35] Myles A J, Feudale R N, Liu Y, *et al*. An introduction to decision tree modeling. J Chemom, 2004, **18**(6): 275-285

[36] Ma Q P, He X L, Li K, *et al*. Dynamic contrast-enhanced ultrasound radiomics for hepatocellular carcinoma recurrence prediction after thermal ablation. Mol Imaging Biol, 2021, **23**(4): 572-585

[37] Li R, Xu X, Lin J, *et al*. Automatic classification of liver cancer in B-ultrasound and contrast-enhanced ultrasound based on convolution neural network. Prog Biochem Biophys, 2023, **50**(3): 668-675

[38] Chen C, Wang Y, Niu J, *et al*. Domain knowledge powered deep learning for breast cancer diagnosis based on contrast-enhanced ultrasound videos. IEEE Trans Med Imaging, 2021, **40**(9): 2439-2451

基于超声造影图像亮度变化曲线的肝细胞癌预测*

陈楹楹[1] 江尚霖[1] 黄良汇[1] 曾亚光[1] 王雪花[1)**] 郑 玮[2)**]

（[1)] 佛山大学物理与光电工程学院，佛山 528225；

[2)] 中山大学肿瘤防治中心超声科，华南肿瘤学国家重点实验室，肿瘤医学省部共建协同创新中心，广州 510060）

摘要 目的 本研究旨在建立一种基于超声造影（CEUS）图像的亮度变化曲线来分类肝细胞癌（HCC）与非HCC恶性肿瘤的方法。**方法** 本研究回顾性地纳入131例HCC患者和30例非HCC恶性肿瘤患者。首先，采用YOLOX网络自动检测B超和超声造影图像中感兴趣的肿瘤区域；然后，开发一种定制算法从超声造影感兴趣区域提取肿瘤及邻近肝实质区域的亮度随时间变化的曲线；最后，构建基于深度学习的一维卷积神经网络（1D-ResNet、1D-ConvNeXt和1D-CNN）和传统的机器学习模型组，包括支持向量机、集成学习、k近邻和决策树等，来分析亮度变化曲线，并对HCC和非HCC恶性肿瘤进行分类。**结果** 各机器学习方法的受试者工作特征曲线下面积（*AUC*）值分别为0.70、0.56、0.63、0.72；1D-ResNet、1D-ConvNeXt和1D-CNN的*AUC*分别为0.72、0.82和0.84。**结论** 1D-CNN可以实现基于亮度变化曲线自动分类HCC和非HCC恶性肿瘤，其准确率高于传统的机器学习方法和其他一维深度学习模型。本文提供了一种简单、低成本的计算机辅助诊断方案来协助放射科医生进行临床诊断HCC。

关键词 计算机辅助诊断，深度学习，肝细胞癌，对比度增强超声，亮度变化曲线

中图分类号 R445.1，TP391.7 **DOI**：10.16476/j.pibb.2024.0517 **CSTR**：32369.14.pibb.20240517

---

* 国家自然科学基金（62075042，62205060，82202179），广东省医学科技研究基金（A2020306）和广东省大学生科技创新培养专项基金（pdjh2024a387）资助。

** 通讯联系人。

王雪花 Tel：0757-82716895，E-mail：xhwang10000@163.com

郑玮 Tel：020-87343212，E-mail：zhengwei@sysucc.org.cn

收稿日期：2024-12-11，接受日期：2025-04-27